Letter Vol. 49, No. 5 / 1 March 2024 / Optics Letters 1241

External chirality enhancing downconversion in a waveguide-coupled nonlinear plasmonic metasurface

Tsafrir Abir,[1,2,*] Symeon Sideris,[2,3] and Tal Ellenbogen[2,3]

[1] Raymond and Beverly Sackler Faculty of Exact Sciences, School of Physics and Astronomy, Tel-Aviv University, Tel-Aviv 6779801, Israel
[2] Center for Light–Matter Interaction, Tel-Aviv University, Tel-Aviv 6779801, Israel
[3] Department of Physical Electronics, School of Electrical Engineering, Tel-Aviv University, Tel Aviv 6997801, Israel
*tsafrirabir@mail.tau.ac.il

Received 16 October 2023; revised 27 January 2024; accepted 28 January 2024; posted 5 February 2024; published 27 February 2024

Metasurfaces, typically constructed from spatial arrangements of localized building blocks, can enhance light–matter interactions through local field enhancement or by coherent coupling to extended photonic modes. Recent works have explored how guided mode resonances influence the performance of nonlinear metasurfaces. Here we investigate the modal impact on difference-frequency generation in a waveguide-coupled metasurface platform. The system is constructed from gold split-ring resonators on a high-index TiO_2 waveguide. We find that a symmetric configuration of the metasurface's localized modes and the extended waveguide modes lead to a modest enhancement of the downconversion process. However, when the mirror symmetry of the localized modes with respect to the guided mode propagation breaks, it introduces external chirality. This enables coupling to a higher quality mode, resulting in a 70-fold enhancement of the difference-frequency generation. The capacity to manipulate the nonlocal modes through the design offers broader control over the interaction and new avenues to tailor the nonlinear processes.

https://doi.org/10.1364/OL.507953

In the realm of nonlinear optical materials, substantial research has been devoted to nonlinear frequency conversion from plasmonic metasurfaces [1]. The sub-wavelength metallic structures are engineered to sustain localized surface plasmon resonances (LSPRs) at specific target frequencies and polarizations, which amplify and modulate the nonlinear optical processes [2]. Practically, the resonances of these meta-atoms can rarely be considered completely local, either due to near-field interactions with their neighbors or by interacting with external and spatially extended optical modes. In recent years, multiple works have been devoted to harnessing nonlocality for wider functionality and better performance in both linear [3] and nonlinear regimes [4].

A metasurface may become nonlocal in the presence of in-plane propagating modes. As the spectrally broad localized modes of the meta-atoms coherently scatter into a surface wave, they spatially extend and become spectrally narrow in the reciprocal space. This is associated with the Rayleigh anomaly (RA) [5], and the extended modes are termed surface lattice resonances (SLRs). To excite the SLRs, especially by normal incidence excitation, it is important to embed the metasurface in a homogeneous dielectric environment [6].

For frequency conversion processes, SLRs were demonstrated to increase the second harmonic generation (SHG) [7–9], third harmonic generation [10,11], and other nonlinear frequency conversion processes [12].

A different path for obtaining collective nonlocal resonances is with the support of guided modes. A periodic structure may diffract and couple to a guided mode, leading to a nonlocal guided mode resonance (GMR) [13]. Recently, the contribution of such a GMR-induced nonlocality to the SHG originating from a nonlinear metasurface was demonstrated [14]. In addition, it has been experimentally shown how GMR enhances entangled photon pair generation from spontaneous parametric downconversion in a thin nonlinear waveguiding slab of $LiNbO_3$ [15].

Here, we focus on the potential enhancement of the unexplored yet difference-frequency generation (DFG) process and study the role of symmetry of the localized modes with respect to the extended modes on the enhancement process. Specifically, we study two different configurations. The first has a mirror symmetry with respect to the plane of incidence, while the second breaks this symmetry. Breaking the mirror symmetry in the plane transverse to the guided modes' propagation results in extrinsic chirality that provides a mixed-polarization response [16].

As mentioned, nonlocality in periodic structures is achieved through extended modes of the structure. The discrete translation symmetry leads to an added quanta of in-plane quasi-momentum

$$\mathbf{k}^{s}_{m_1,m_2} = \mathbf{k}^{s}_{\mathrm{inc}} + m_1\mathbf{b}_1 + m_2\mathbf{b}_2 \,, \tag{1}$$

where $\mathbf{k}_{\mathrm{inc}}$ is the incident field's wave vector, $\mathbf{b}_i$ are the reciprocal lattice vectors, and m_i are integers. $\mathbf{k}_{m_1,m_2}$ is the wave vector of the collective scattered field, i.e., the diffraction of order (m_1, m_2). The s superscript refers to the vectors' projection on the metasurface's plane.

The formation of a GMR requires that $|\mathbf{k}^{s}_{m_1,m_2}|$ is matched with the propagation constant of a guided mode. If the metasurface weakly perturbs the waveguide, the guided modes' dispersions

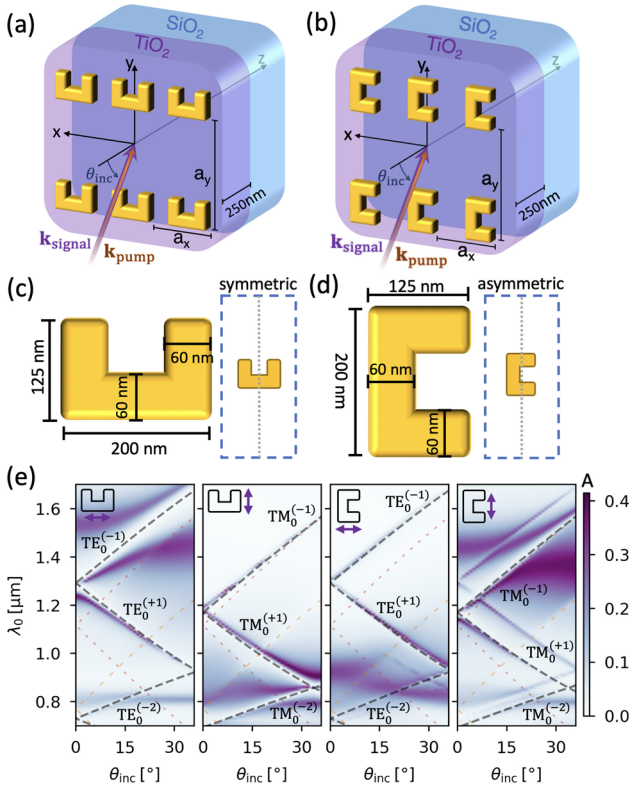

Fig. 1. Systems' description and linear response. (a) and (b) illustrate the two studied configurations of metasurface on a TiO_2 waveguiding slab. (c) and (d) depict the dimensions of individual gold SRR, with their orientation within the unit cell for the two configurations. (e) Angle-dependent absorptance spectra with the labeled GMRs dispersion, where the two left panels show the results for the symmetric configuration and the two on the right show the absoptance of the asymmetric configuration. The four share the same vertical axis and colormap, with the purple arrows indicating the orientation of the polarizations with respect to the SRRs. The GMRs are plotted solely for the incident field's polarization for brevity and despite the apparent cross-polarization response of the asymmetric configuration. Polarization-independent RAs are marked by the colored dashed lines.

can be approximated by that of a bare waveguide. For a simple high-index slab, the guided mode dispersion is obtained by solving transcendental equations [14], whereas tuning of the GMRs is possible by modifying the waveguide design and the metasurface's periodicity.

For our study, we simulate the aforementioned process using the finite element method. Bloch boundary conditions are used to infinitely extend the structure to the lateral dimensions while perfectly matched layers are placed in the other dimension to terminate the computational domain. The waveguiding structure in our study is a 250 nm thick TiO_2 film on a fused silica substrate. The higher index of the TiO_2 layer (n = 2) with respect to the fused silica (n = 1.45) and air (n = 1) acts as the waveguiding layer, which supports the guided modes. The 50 nm thick gold split-ring resonators' (SRRs) metasurface lies on top of the high-index waveguiding layer, as depicted in Figs. 1(a) and 1(b) for the symmetric and asymmetric configurations, respectively. The SRRs' lateral dimensions are portrayed in Figs. 1(c) and 1(d), where the asymmetric configuration has its SRRs rotated by 90°. Both systems under study have identical rectangular unit-cells defined by the lattice spacings $a_x = 350$ nm, and $a_y = 770$ nm to support GMRs propagating in the $\hat{y}$ direction. We take the y–z plane as the plane of incidence, i.e., the azimuthal angle set to 90°. Due to the inherent broken inversion symmetry of these designs owing to the SRRs' geometry, these waveguide platforms are suitable for quadratic nonlinear frequency conversion processes [17].

First, we consider the polarization-dependent linear response conveyed in the resulting absorptance $A = 1 - T - R$, where T and R are, respectively, the specular transmittance and reflectance, as it accounts for both the losses and the power that remains bound to the waveguide. Figure 1(e) presents simulated angle-dependent absorptance spectra for TE and TM polarizations and the calculated GMRs' dispersion. Since the optical response is the same for the negative and positive θ_{inc}, the results are presented only for positive angles. The GMRs are labeled with a subscript indicating the guided mode's order and a superscript for the diffraction order. The localized modes of the metasurface are the dispersionless–horizontal features, which exhibit a mode-splitting behavior when spectrally overlap with a GMR, a behavior commonly observed in coupled systems. Cross-polarization response is evident in the two right panels of Fig. 1(e) presenting the results of the asymmetric configuration. That is, when the incident wave is purely TE or TM polarized, GMRs of the orthogonal polarization are also present. The red and orange dispersion lines follow the vague spectral features related to the polarization-independent RA of the substrate and free space, respectively.

Next, we proceed to the analysis of the DFG. The frequency conversion on the gold SRRs originates from the highly nonlinear free-electron dynamics in the plasmonic structure. One model that provides an adequate description of the charge dynamics is the hydrodynamic model under the Thomas–Fermi approximation [18,19]. This quasi-classical model has been found to capture the optical properties of structures with high concentrations of free carriers. It describes the results for various nonlinear optical processes such as second harmonic, third harmonic, and even THz generation [20–22]. Recently, it even assisted in revealing the role of indium–tin-oxide in enhancing plasmonic metasurfaces' nonlinear response [23,24].

In our work, we follow the results of De Luca and Ciracì [25], expressing the nonlinear surface currents responsible for DFG. For the incident pump and signal harmonic fields $\mathbf{E}_1(\omega_1)$ and $\mathbf{E}_2(\omega_2)$, respectively, the nonlinear surface current associated with the idler frequency $\omega_3 = \omega_1 - \omega_2$ is given by

$$\begin{aligned}\mathbf{K}_3^{\mathrm{NL}} = \frac{i}{\omega_3 + i\gamma} \Bigg(\hat{\mathbf{t}} \Bigg[\frac{e}{m}\left(P_{1,b}^{\perp} E_2^{\parallel *} + P_{2,b}^{\perp *} E_1^{\parallel}\right) \\ + \frac{2\omega_1\omega_2}{e n_0}\left(P_{1,b}^{\perp} P_2^{\parallel *} + P_{2,b}^{\perp *} P_1^{\parallel}\right) \Bigg] \\ + \hat{\mathbf{n}} \Bigg[\frac{\varepsilon_0 e}{m}\left(E_{1,b}^{\perp} E_{2,b}^{\perp *} - E_{1,o}^{\perp} E_{2,o}^{\perp *}\right) \\ + \frac{2\omega_1\omega_2}{e n_0} P_{1,b}^{\perp} P_{2,b}^{\perp *} \Bigg] \Bigg) ,\end{aligned} \tag{2}$$

where $\hat{\mathbf{t}}$ and $\hat{\mathbf{n}}$ are unit vectors parallel and perpendicular to the surface, respectively. γ is the metal's loss, and $\mathbf{P}_i$ represents its polarization in response to the incident field $\mathbf{E}_i$. m and e are the electron mass and charge, respectively, and n_0 is the free-electron density in the metal. The superscripts $\parallel$ and $\perp$ indicate the surface parallel and perpendicular components of the fields, respectively. The fields normal to the surface are discontinuous;

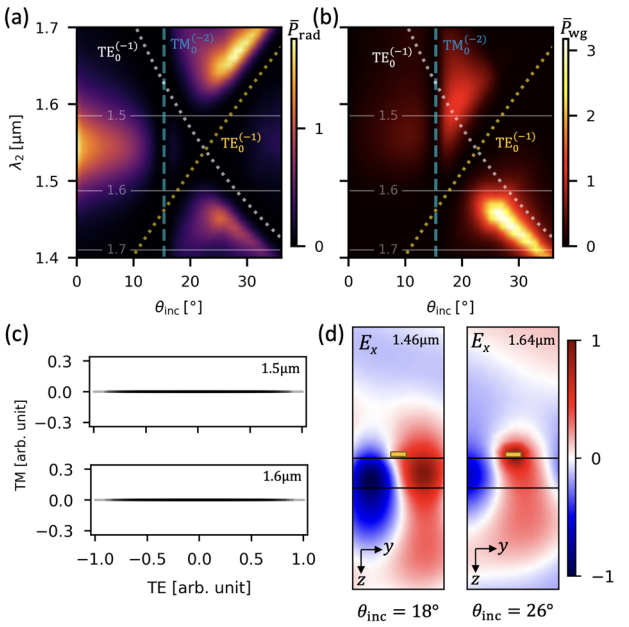

Fig. 2. DFG characterization. (a) Power enhancement of the DFG radiating from the metasurface-waveguide structure. (b) The power enhancement of the confined DFG. In both (a) and (b) θ_{inc} and λ_2 are varied while keeping $\lambda_1 = 0.77\mu m$, and resulting values of λ_3 are indicated by the horizontal lines. The vertical dashed line is the GMRs for λ_1, while the dotted white and gold lines mark the GMRs' dispersion for λ_2 and λ_3, respectively. (c) Sampled polarization state of the radiated DFG at λ_3 indicated in the top-right corner. The polarization is sampled for the range of the angles and overlaid one another. (d) Sampled normalized TE near-field.

therefore, the subscripts b and o are used to define whether the evaluation is performed on the bulk side of the surface or outside of it.

For the DFG study, the separate solutions for the pump and signal fields are combined using Eq. (2) to obtain $\mathbf{K}_3^{NL}$, which acts as a source for the new frequency. In our analysis, we fix the pump wavelength $\lambda_1 = 0.77$ μm and take it to be TM/TE polarized for stronger absorptance for the symmetric/asymmetric configuration (respectively), as implied from Fig. 1(e). The orthogonally polarized signal input field varies in λ_2 together with θ_{inc} to map the GMRs' effect on the nonlinear response. In the following section, we start by describing the results obtained from the symmetric configuration. The results are presented for positive θ_{inc}, while for negative angles, the results are mirrored with opposite signs of diffraction orders and counter-propagating guided modes.

Initially, we consider the DFG power radiating away from the sample by summing the 0^{th}-order diffraction to the substrate and superstrate. To provide a measure for the DFG enhancement $\bar{P}_{rad}(\omega_3)$, it is normalized by the highest power generated by the same metasurface lying on a TiO_2 substrate, without any guided mode contributions. The results are presented in Fig. 2(a) with the GMR dispersion. The dashed yellow line tracks the dispersion of the $TE_0^{(-1)}$ GMR for λ_2, while the white dotted line does the same for λ_3 (horizontal white lines). The vertical dashed blue line marks θ_{inc} in which $TM_0^{(-2)}$ GMR condition holds for λ_1. These are the same modes found in the absorptance spectra in Fig. 1(e). It is clear how the frequency conversion diminishes along these lines. For the pump and signal, this is a result of destructive interference between the collective scattered field and the incident field. In contrast, for the idler, the dip results from the coupling of the power to the waveguiding structure.

To further validate that, we probe the power propagating within the waveguiding layer. The results are presented in Fig. 2(b) using the same normalization for the evaluation of the DFG enhancement $\bar{P}_{wg}(\omega_3)$. We observe it peaks along the GMR associated with the idler, while lessening when overlapped with GMRs of the input fields. Additionally, $\bar{P}_{wg}(\omega_3)$ increases at steeper incident angles, and this is attributed to two contributions implied from Fig. 1(e). The first is an improved extinction of the signal. The second comes from the increased quality of the idler's nonlocal mode as it becomes less susceptible to the LSPR's loss.

The dependence of the DFG on TE-polarized GMR suggests it is TE-polarized as well. To analyze its polarization state, Stoke's parameters are calculated from the fields radiating away from the structure. These are used to plot multiple polarization ellipses for two values of λ_3 (Fig. 2(c)). The ellipses are sampled at each discrete θ_{inc} and overlayed on one another with the opacity determined by the idler's intensity. The TE nature of the idler is also indicated by its near-field, illustrated in Fig. 2(d) for two points picked from the areas of enhancement seen in Fig. 2(b). Overall, it is clear how the polarization remains purely TE polarized, regardless of θ_{inc} and ω_3.

While the effects of nonlocal modes are obviously seen, the enhancement of the nonlinear conversion process is very modest, with less than two-fold for the radiated power and about three-fold within the waveguide. We proceed to our analysis of the asymmetric design and discuss how the external chirality may contribute.

The mixed-polarization response leads to spectral features related to GMRs of both polarizations for all involved frequencies. In Fig. 3(a), GMRs appear as dips, yet they are spectrally narrower than those seen in Fig. 2(a). Near the dips and where modes intersect, slightly higher values of DFG enhancement are seen, stemming from the increase of light–matter interaction in the nonlocal modes of the metasurface. If we examine the power confined to the waveguide depicted in Fig. 3(b), a much larger enhancement is obtained, peaking at 70 times larger compared to the same metasurface without nonlocal contributions. We note how it follows the TE polarized GMR, as it benefits from a better confined and higher quality mode. The results in Figs. 1(e) and 3(a) further indicate how TE GMRs are of higher quality than the TM GMRs at the idler's wavelength range.

Now, the polarization of the idler is not as straightforward as in the first design. The radiated DFG is no longer entirely linearly polarized, as depicted by the polarization ellipses in Fig. 3(c). We notice it is mostly TM polarized, favoring the polarization of $\mathbf{E}_2$, and that of the LSPR excited along the base of the SRR. However, the external chirality enables polarization mixing, and the waveguide-bound DFG is mainly enhanced along the $TE_0^{(-1)}$. Deviating from the TE mode results in a Stark decrease in power, and it becomes mostly TM polarized, as indicated by the field arrows in Fig. 3(d). Surprisingly, despite the TM tendency of the DFG in this configuration, most of the enhancement within the waveguide is achieved for the TE polarization.

In conclusion, this study explores the implementation of plasmonic metasurfaces with a planar waveguide to enhance light–matter interactions for the processes of DFG. Using frequency domain simulations employing the hydrodynamic model, we explored two configurations. We observe how

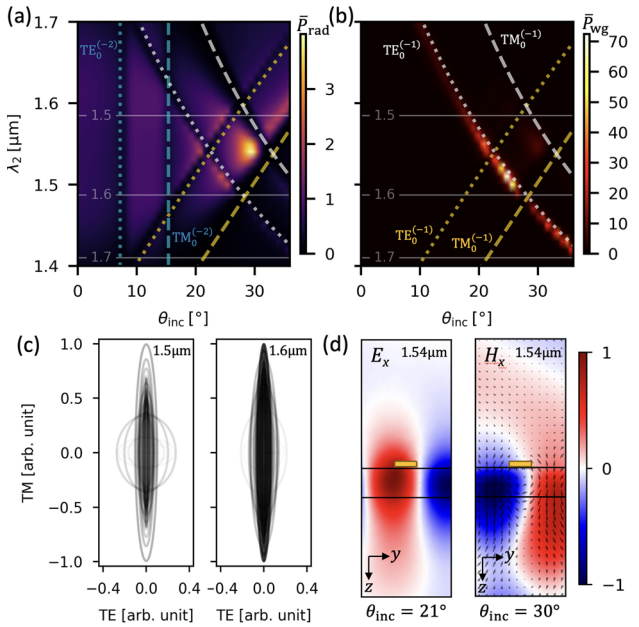

Fig. 3. DFG characterization for the rotated SRRs design. (a) Power enhancement of the DFG radiating from the metasurface-waveguide structure. (b) Power enhancement of the confined DFG. The dispersion lines for λ_1 appear only in (a), while GMRs for $\lambda_{2,3}$ are labeled only in (b). (c) Polarization state of the radiated DFG is sampled at different angles at a specific wavelength indicated in the top-right corner. (d) Normalized near-field for TE (left) and TM (right), the arrows indicate the orientation of $\mathbf{E}(\omega_3)$ for the TM polarization.

improved absorptance for the pump and signal waves contributes to the frequency conversion, while for the idler, it is better to avoid loss and couple with spectrally sharp nonlocal modes. Introducing extrinsic chirality and a mixed-polarization response enables the coupling into a higher quality GMR, enhancing the DFG by an order of magnitude. These findings present valuable insights into the potential of nonlocal and nonlinear metasurfaces in manipulating light on the nanoscale, opening up new possibilities for photonic applications. Moreover, the large number of design parameters enables optimization and allows the exploration of other DFG-related processes, such as optical parametric oscillations and amplification.

Funding. Israel Science Foundation (581/19).

Disclosures. The authors declare no conflicts of interest.

Data availability. Data underlying the results presented in this paper are not publicly available at this time but may be obtained from the authors upon reasonable request.

REFERENCES

1. A. Krasnok, M. Tymchenko, and A. Alù, Mater. Today **21**, 8 (2018).
2. S. Keren-Zur, L. Michaeli, H. Suchowski, *et al.*, Adv. Opt. Photonics **10**, 309 (2018).
3. A. Overvig and A. Alù, Laser Photonics Rev. **16**, 2100633 (2022).
4. R. Kolkowski, T. K. Hakala, A. Shevchenko, *et al.*, Appl. Phys. Lett. **122**, 160502 (2023).
5. F. J. García De Abajo, Rev. Mod. Phys. **79**, 1267 (2007).
6. B. Auguié and W. L. Barnes, Phys. Rev. Lett. **101**, 143902 (2008).
7. R. Czaplicki, A. Kiviniemi, J. Laukkanen, *et al.*, Opt. Lett. **41**, 2684 (2016).
8. L. Michaeli, S. Keren-Zur, O. Avayu, *et al.*, Phys. Rev. Lett. **118**, 243904 (2017).
9. R. Czaplicki, A. Kiviniemi, M. J. Huttunen, *et al.*, Nano Lett. **18**, 7709 (2018).
10. O. Doron, L. Michaeli, and T. Ellenbogen, J. Opt. Soc. Am. B **36**, E71 (2019).
11. J. Gour, S. Beer, A. Alberucci, *et al.*, Opt. Lett. **47**, 6025 (2022).
12. M. J. Huttunen, P. Rasekh, R. W. Boyd, *et al.*, Phys. Rev. A **97**, 053817 (2018).
13. G. Quaranta, G. Basset, O. J. F. Martin, *et al.*, Laser Photonics Rev. **12**, 1800017 (2018).
14. T. Abir, M. Tal, and T. Ellenbogen, Nano Lett. **22**, 2712 (2022).
15. J. Zhang, J. Ma, M. Parry, *et al.*, Sci. Adv. **8**, eabq4240 (2022).
16. K. Achouri, V. Tiukuvaara, and O. J. F. Martin, Adv. Photonics **5**, 1 (2023).
17. M. W. Klein, C. Enkrich, M. Wegener, *et al.*, Science **313**, 502 (2006).
18. A. V. Krasavin, P. Ginzburg, and A. V. Zayats, Laser Photonics Rev. **12**, 1700082 (2018).
19. N. A. Mortensen, Nanophotonics **10**, 2563 (2021).
20. C. Ciracì, E. Poutrina, M. Scalora, *et al.*, Phys. Rev. B **85**, 201403 (2012).
21. C. Ciracì, M. Scalora, and D. R. Smith, Phys. Rev. B **91**, 205403 (2015).
22. S. Sideris and T. Ellenbogen, Opt. Lett. **44**, 3590 (2019).
23. S. Sideris, E. Minerbi, C. McDonnell, *et al.*, ACS Photonics **9**, 3981 (2022).
24. E. Minerbi, S. Sideris, J. B. Khurgin, *et al.*, Nano Lett. **22**, 6194 (2022).
25. F. De Luca and C. Ciracì, J. Opt. Soc. Am. B **36**, 1979 (2019).